

VideoLifter: Lifting Videos to 3D with Fast Hierarchical Stereo Alignment

Wenyan Cong¹, Kevin Wang¹, Jiahui Lei², Colton Stearns³, Yuanhao Cai⁴, Dilin Wang⁵,
Rakesh Ranjan⁵, Matt Feiszli⁵, Leonidas Guibas³, Zhangyang Wang¹, Weiyao Wang⁵, Zhiwen Fan¹
¹UT Austin ²UPenn ³Stanford ⁴JHU ⁵Meta

Project Website: <https://videolifter.github.io>

Abstract

Efficiently reconstructing accurate 3D models from monocular video is a key challenge in computer vision, critical for advancing applications in virtual reality, robotics, and scene understanding. Existing approaches typically require pre-computed camera parameters and frame-by-frame reconstruction pipelines, which are prone to error accumulation and entail significant computational overhead. To address these limitations, we introduce VideoLifter, a novel framework that leverages geometric priors from a learnable model to incrementally optimize a globally sparse to dense 3D representation directly from video sequences. VideoLifter segments the video sequence into local windows, where it matches and registers frames, constructs consistent fragments, and aligns them hierarchically to produce a unified 3D model. By tracking and propagating sparse point correspondences across frames and fragments, VideoLifter incrementally refines camera poses and 3D structure, minimizing reprojection error for improved accuracy and robustness. This approach significantly accelerates the reconstruction process, reducing training time by over 82% while surpassing current state-of-the-art methods in visual fidelity and computational efficiency.

1. Introduction

Efficiently reconstructing 3D scenes from sequential image observations is a longstanding challenge in computer vision, with applications spanning virtual and augmented reality (VR/AR), video processing, outdoor photogrammetry, autonomous driving, urban planning, and medical imaging. Recently, reconstructing 3D scenes from single video sequences has gained significant traction. This trend is driven by two factors: the increasing accessibility of handheld capture devices, which makes video capture more practical for non-professional users, and recent advancements in high-fidelity 3D reconstruction techniques from images. Notable examples include Neural Radiance Fields (NeRF) [26] and

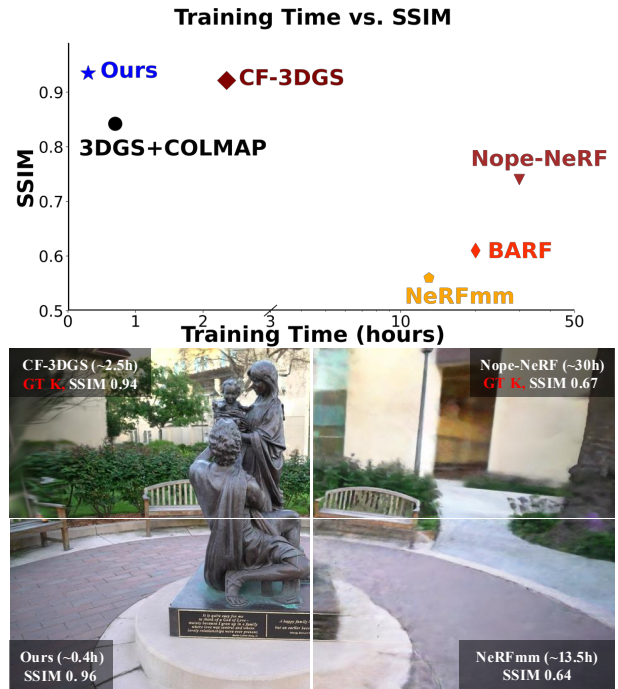


Figure 1. **Novel View Synthesis and Training Time Comparisons.** VideoLifter does not require precomputed camera parameters (i.e., camera intrinsics K from COLMAP), reduces the training time required by the most relevant baseline CF-3DGS by 82% while improving image quality (SSIM) by 0.2.

3D Gaussian Splatting [18], which have expanded the possibilities for capturing complex, high-quality 3D representations from image data.

Most video-to-3D reconstruction methods, either based on radiance fields or Gaussian splatting, heavily depend on Structure-from-Motion (SfM) [32] to generate initial sparse reconstructions, providing essential components like camera poses, intrinsics, and an initial point cloud to build dense 3D models. However, in video data, SfM is *not reliable or even approachable* (**Issue** ①) due to its reliance on photo-

metric assumptions that often fail in low-texture or challenging lighting conditions [24, 27, 32].

To address the limitations of traditional SfM, recent methods [6, 12, 21, 42] have shifted toward jointly optimizing camera poses and scene representations rather than relying on initial sparse reconstructions from SfM. These methods generally show a working manner of incrementally reconstructing scenes from a canonical view. However, they face several significant limitations: (a) *Lack of Robustness (Issue ②)*: they still rely on accurate camera intrinsics from SfM, which makes them unreliable when applied to in-the-wild video data. (b) *Slow and Inefficient (Issue ③)*: these methods are very slow due to their iterative, frame-by-frame approach requiring re-optimizing the entire sequence with each new frame. Moreover, for camera pose optimization, they assume constant-velocity camera motion and also re-optimize camera poses from scratch, which prolongs training times and complicates handling complex trajectories. (c) *Susceptibility to Incremental Errors (Issue ④)*: in long video sequences, the frame-by-frame approach makes these methods prone to cumulative errors.

To address the limitations of existing methods, we propose VideoLifter, a novel approach for **efficient** and **robust** video-to-3D reconstruction that operates **without the need for SfM**. Our method follows the typical sparse-to-dense strategy with two key innovations: (1) **Sparse point-based fragment registration**: inspired by hierarchical SfM [34], we capture a sparse scene representation from video data by dividing the input video into non-overlapping fragments anchored by key frames. We construct an efficient subgraph from these key frames to optimize anchor point clouds, providing shared camera intrinsics and transformation matrices across fragments. Local camera extrinsics within each fragment are estimated through sparse feature matching, leveraging pretrained geometric priors from foundation model (e.g. MAST3R [20]) and *eliminating the need for precomputed camera poses or intrinsic from unreliable SfM* (Issue ① ②). (2) **Hierarchical 3D Gaussian alignment**: for dense 3D reconstruction, we address *cumulative errors* (Issue ④) over long video sequences by introducing a hierarchical approach. Starting with the registered fragments, local 3D Gaussians are initialized and optimized based on photometric consistency. These local representations are then hierarchically merged into a unified scene representation, ensuring global consistency and accurate camera pose alignment.

By leveraging our fragment-by-fragment and hierarchical strategy, VideoLifter achieves both high computational efficiency and high quality renderings when handling video sequences (Issue ③). Moreover, the lack of reliance on precomputed camera parameters or SfM makes our approach highly robust and flexible. As shown in Fig. 1, VideoLifter achieves $> 5\times$ **speed** improve-

ments and **enhanced view-synthesis quality** compared to various state-of-the-art methods.

Overall, our main contributions are as follows:

- We introduce VideoLifter, an efficient, flexible, and robust video-to-3D reconstruction framework, reinventing the sparse-to-dense reconstruction strategy with two novel stages.
- Our **sparse point-based fragment registration** efficiently captures the sparse representation for long-sequence videos in a fragment-by-fragment manner, utilizing a learnable model for geometric priors without relying on SfM, ensuring robustness across video data.
- Our **hierarchical 3D Gaussian alignment** minimizes incremental errors while significantly enhancing reconstruction speed, achieving more than $5\times$ speed improvements over existing methods.
- Extensive experiments on the Tanks and Temples and CO3D-V2 datasets demonstrate that VideoLifter significantly improves training efficiency and rendering quality compared to state-of-the-art methods.

2. Related Works and Preliminary

3D Representations for Novel View Synthesis 3D reconstruction for high-quality novel view synthesis is the task of generating unseen views of a scene or object from a set of given images [1, 25]. One of the most influential methods, Neural Radiance Fields (NeRF) [26], introduced the use of multilayer perceptrons (MLPs) to represent 3D scenes. By taking the 3D coordinates and viewing directions as input and utilizing volume rendering techniques, NeRF achieves photo-realistic image synthesis. However, despite its ability to produce high-quality renderings, NeRF is computationally expensive and slow, both during training and inference. Research following NeRF has aimed at either improving the quality of renderings [2–4] or boosting the efficiency of the approach [30, 33, 36, 37], though few methods succeed in addressing both quality and efficiency simultaneously. This is largely due to the inherently ill-posed nature of transforming a sparse point cloud into a dense 3D scene representation. In recent years, unstructured radiance field methods have emerged [7, 18, 44], using different scene representation primitives. Among these, 3D Gaussian Splatting (3D-GS)[18] stands out by employing anisotropic 3D Gaussians[46] to model radiance fields. This technique, combined with differentiable splatting for rendering, has demonstrated impressive performance in efficiently reconstructing complex, real-world scenes with high fidelity. However, 3D-GS performs the sparse-to-dense optimization starting from structure-from-motion point clouds, named adaptive density control, which is critical for converting sparse point clouds into dense 3D Gaussian representations. A notable limitation is that the optimization of SfM and the subsequent 3D Gaussian re-

finement are decoupled, which can lead to the accumulation of errors that the current pipelines are unable to correct. NeRFs and 3DGS rely on carefully captured sequential video or multi-view images to ensure sufficient scene coverage, utilizing preprocessing tools like Structure-from-Motion (SfM) software such as COLMAP [32] to compute camera parameters and provide a sparse SfM point cloud as additional input.

Traditional Structure-from-Motion (SfM) Estimating 3D structure and camera motion simultaneously is a well-explored challenge, with a long-established set of techniques addressing the problem [13, 29, 43]. Structure from Motion (SfM) has seen significant advancements across various dimensions. Methods like [15, 22] focus on enhancing feature detection, while [35] introduces innovative optimization approaches. Improved data representations and more robust structural solutions are explored by [14, 32]. Simultaneous Localization and Mapping (SLAM) systems, on the other hand, track camera motion and construct 3D structures from video sequences [9, 28, 29]. In [9], the photometric bundle adjustment algorithm is proposed, which directly minimizes photometric errors by aligning pixels. Despite these advances, traditional SfM and SLAM techniques remain vulnerable to issues such as low-texture regions, occlusions, moving objects, and lighting variations, limiting their overall robustness and performance.

Radiance Field without SfM The limitations of SfM—particularly in handling textureless surfaces, motion blur, or specular reflections—can lead to cumulative errors that propagate through subsequent stages of radiance field reconstruction, reducing overall accuracy. To overcome these issues, several approaches have been proposed to eliminate the reliance on SfM during the optimization of radiance fields. NeRFmm [42], for example, jointly optimizes camera intrinsics, extrinsics, and radiance field training, bypassing the need for pre-computed poses. Similarly, BARF [21] adopts a coarse-to-fine pose refinement strategy while jointly optimizing NeRF to handle pose inaccuracies. SCNeRF [16] incorporates a parameterization of camera distortions and utilizes geometric loss to regularize ray tracing. GARF [16] further simplifies joint pose and scene optimization by leveraging Gaussian-MLP models to improve both efficiency and accuracy. SPARF [39] and TrackNeRF [23] introduces a method to simulate pose noise by injecting Gaussian noise into the camera parameters. More recent work integrates depth information as an additional constraint to refine radiance field and 3DGS optimization. Nope-NeRF [6], Lu-NeRF [8], LocalRF [24], and CF-3DGS [12] all utilize depth data to guide the optimization process. Pushing the envelope further, new techniques such as the work in [17] and InstantSplat [10] employ monocular depth estimators

and image-matching networks, and integrate end-to-end stereo models like DUST3R [40] to reduce the dependency on camera pose information. While these methods show promise in reducing the number of views required for accurate scene reconstruction, scaling them effectively to a large number of views remains a challenge.

3D Gaussian Splatting 3D Gaussian Splatting [18] is an explicit 3D scene representation utilizing a set of 3D Gaussians to model the scene. A 3D Gaussian is parameterized by a mean vector $\mathbf{x} \in \mathbb{R}^3$ and a covariance matrix $\Sigma \in \mathbb{R}^{3 \times 3}$:

$$G(\mathbf{p}) = \frac{1}{(2\pi)^{3/2} |\Sigma|^{1/2}} e^{-\frac{1}{2}(\mathbf{p}-\mathbf{x})^T \Sigma^{-1} (\mathbf{p}-\mathbf{x})} \quad (1)$$

To represent the view-direction-dependent, spherical harmonic (SH) coefficients are attached to each Gaussian, and the color is computed via $\mathbf{c}(\mathbf{d}) = \sum_{i=1}^n \mathbf{c}_i \mathcal{B}_i(\mathbf{d})$, where \mathcal{B}_i is the i^{th} SH basis. And the color is rendered via $\mathbf{c} = \sum_{i=1}^n \mathbf{c}_i \alpha_i \prod_{j=1}^{i-1} (1 - \alpha_j)$, where \mathbf{c}_i is the color computed from the SH coefficients of the i^{th} Gaussian. α_i is given by evaluating a 2D Gaussian with covariance multiplied by a learned per-Gaussian opacity. The 2D covariance matrix is calculated by projecting the 3D covariance to the camera coordinates. The 3D covariance matrix is decomposed into a scaling matrix and a rotation matrix and is optimized as Gaussian attributes.

3. VideoLifter: An Efficient and Effective Video-to-3D Framework

We first start with the definition of the targeted video-to-3D reconstruction problem that VideoLifter solves.

Problem Given a sequence of N unposed and uncalibrated images from a monocular video, denoted as $\mathcal{I} = \{I_i \in \mathbb{R}^{H \times W \times 3}\}_{i=1}^N$, VideoLifter reconstructs the scene using 3D Gaussians \mathcal{G} along with estimated camera intrinsics K and extrinsics $\mathcal{T} = \{T_i \in \mathbb{R}^{3 \times 4}\}_{i=1}^N$. Here, we assume all frames share a common intrinsic matrix, as a single monocular video capture is the input.

Challenges Existing frameworks often rely on a frame-by-frame approach, making them inherently **slow** and **prone to cumulative errors** when processing videos. Furthermore, these methods depend on Structure-from-Motion for camera intrinsics, which can be **unreliable** or even infeasible for in-the-wild video data due to low texture, inconsistent lighting, or motion blur.

Our High-level Framework To ensure both efficiency and effectiveness while handling video data, we propose a novel sparse-to-dense reconstruction pipeline, as illustrated in Fig. 2. The pipeline integrates two key innovations designed for efficiency and robustness:

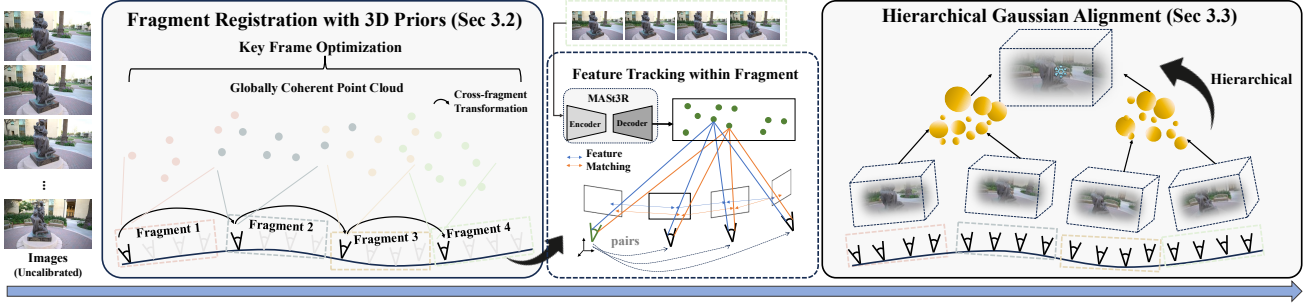


Figure 2. **Network Architecture.** Our method takes uncalibrated images as input and reconstructs a dense scene representation based on self-supervised photometric signals. It performs efficient sparse reconstruction through the use of “feature points” to formulate an initial solution for globally aligned camera poses. It subsequently optimizes a set of 3D Gaussians and corrects erroneous estimations from each fragment, hierarchically aligning them into a globally coherent 3D representation.

- **Sparse Point-Based Fragment Registration with 3D Priors** enables efficient sparse reconstruction in a fragment-by-fragment way and also eliminates reliance on SfM by using 3D priors.
- **Hierarchical 3D Gaussian Alignment** obtains a globally coherent 3D representation in a hierarchical way to both boost efficiency as well as reduce merging error.

3.1. Fragment Registration with Learned 3D Priors

To enable efficient sparse reconstruction, we propose a fragment-by-fragment approach, diverging from conventional methods that process video either frame-by-frame or by optimizing the entire video sequence simultaneously. This design choice significantly enhances the computational efficiency of our pipeline. Specifically, we divide the input sequence into m disjoint windows of length k (referred to as **fragments**). For example, the i 'th fragment would be $\mathcal{I}_i^f = [I_{(i-1)k+1}, I_{(i-1)k+2}, \dots, I_{ik}]$, where $i \in [1, m]$.

To process data in a fragment-by-fragment manner, it is essential to extract both intra-fragment and inter-fragment informative features. For intra-fragment processing, we estimate the locally aligned camera extrinsics \mathcal{T}_i^f , within fragment \mathcal{I}_i^f , using the sparse point cloud:

$$\mathcal{T}_i^f = \text{Frag-Regis}(\mathcal{I}_i^f, f_{\text{prior}}(\mathcal{I}_i^f)), \quad i \in [1, m],$$

where f_{prior} refers to the SfM which is widely used to initialize reconstruction. However, due to the inefficiency and unreliability of SfM in video settings, we propose leveraging a large-scale 3D model to obtain robust 3D geometric priors [20].

Furthermore, to ensure the consistency of point clouds between adjacent fragments, we “anchor” each fragment using its first frame, $I_{(i-1)k+1}$, referred to as the **key frame**. Key frames are used to obtain a globally consistent optimized dense point map, as well as intrinsic K and transformation matrices across adjacent fragments $\{\mathcal{T}_{i \rightarrow i+1}^f\}_{i=1}^{m-1}$.

Model Inter-Fragment Consistency with Efficient Key Frame Optimization Processing the video in a fragment-wise manner, rather than frame-by-frame, requires careful handling of inter-fragment consistency, since each fragment independently estimates its extrinsics without direct inference from other fragments.

For a monocular video, a straightforward solution to build inter-fragment consistency is to build a complete graph by taking every pair as the input of MAST3R [20] to enforce global consistency. However, rather than constructing a complete graph, we build a more efficient sub-graph by only using key frames and the four closest frames to each key frame. This approach leverages the fact that MAST3R’s stereo predictions are more accurate for pairs with significant co-visibility. Specifically, given a set of key frames $\{I_{(i-1)k+1}\}_{i=1}^m$, where k is the number of views per fragment and m is the number of fragments, we construct a subgraph $\mathcal{G}_m(\mathcal{V}, \mathcal{E})$ to model the relationships among key frames and their neighboring frames. In this subgraph, each vertex $v \in \mathcal{V}$ corresponds to a key frame or one of its four closest neighboring frames, and each edge $e = (v, u) \in \mathcal{E}$ represents shared visual content between frames I_v and I_u .

Key frame optimization is then performed to achieve three objectives: optimized point maps for key frames \tilde{P} , relative transformations \mathbf{T}_e , and a shared focal \bar{f} . Here $\{\mathcal{T}_{i \rightarrow i+1}^f\}_{i=1}^{m-1} \subset \mathbf{T}_e$.

The optimization of the transformation matrix, scaling factor σ_e , and point map) is carried on the efficient sub-graph. Following the procedure in MAST3R, for each image pair $e = (v, u) \in \mathcal{E}$, we denote the point maps $P_{v,v}$ and $P_{u,v}$, along with their confidence maps $O_{v,v}$ and $O_{u,v}$. For clarity, we define $P_{v,e} := P_{v,v}$, $P_{u,e} := P_{u,u}$, $O_{v,e} := O_{v,v}$, and $O_{u,e} := O_{u,u}$. To this end, we optimize

$$(\tilde{P}^*, \mathbf{T}_e^*) = \arg \min_{\tilde{P}, \mathbf{T}, \sigma} \sum_{e \in \mathcal{E}} \sum_{v \in e} \sum_{i=1}^{HW} O_{v,e}^i \left\| \tilde{P}_v^i - \sigma_e \mathbf{T}_e P_{v,e}^i \right\|.$$

Note that this efficient sub-graph could be extended to long video sequences without excessive computational demands, as the complexity of this sub-graph is bounded by $\mathcal{O}(\frac{N}{k} * 4)$, which scales linearly with the number of images N .

With the optimized point map, the focal length for each camera could be further computed following MAST3R:

$$f^* = \arg \min_f \sum_{i=0}^W \sum_{j=0}^H \mathcal{O}^{i,j} \left\| (i', j') - f \frac{(\mathbf{P}^{i,j,0}, \mathbf{P}^{i,j,1})}{\mathbf{P}^{i,j,2}} \right\|.$$

Assuming a single-camera setup for monocular video, similar to COLMAP for single-scene capture, we propose estimating the shared focal length by averaging across all training views: $\bar{f} = \frac{1}{N} \sum_{i=1}^N f_i^*$.

Feature Tracking within Fragment The input video is partitioned into non-overlapping fragments, each containing k frames. Within each fragment, pairwise feature correspondences are established between the key frame and all subsequent frames, reducing the incremental errors commonly encountered in sequential matching.

To refine the camera poses derived from initial pairwise estimates, consider the first fragment $\mathcal{I}_1^f = \{I_1, I_2, \dots, I_k\}$ as an example. We begin by identifying the intersection of 2D correspondences between the key frame I_1 and each subsequent frame from index 2 to k . This process yields a consistent set of correspondences visible across all frames within the same fragment. Using these intersected 2D correspondences, the corresponding 3D positions from the key frame, previously optimized during key frame processing, are retrieved. These 3D-2D correspondences serve as input to PnP-RANSAC [11], refining the camera poses to ensure alignment with consistent 3D points across views in the fragment.

Despite this refinement, scale variations may persist within the point clouds of the fragment due to independent inference. To address this problem, intersected 3D points from the key frame are utilized for scale estimation across all image pairs. Specifically, for each image pair (I_1, I_i) between I_1 and $\{I_i\}_{i=2}^k$, the corresponding 3D point positions (with a total of P points) are retrieved. A one-degree-of-freedom (1-DoF) scale factor is computed between the intersected 3D points in the current pair and those from the key frame:

$$s_i = \arg \min_s \sum_{n=1}^P \|s \mathbf{p}_n^{(i)} - \mathbf{p}_n^{(1)}\|^2. \quad (2)$$

This scale factor is then applied to the dense 3D points of view I_i in the next stage, ensuring local alignment of the point clouds within the fragment and maintaining a consistent scale relative to the key frame. Specifically, the point

map of I_1 is treated as stereo metric depth, since it has already been globally optimized among all key frames, maintaining consistency across fragments.

3.2. Hierarchical Gaussian Alignment

We then perform dense 3D scene reconstruction using Gaussian splatting, ensuring that the final 3D model is both globally coherent while finely capturing local scene details through hierarchical Gaussian alignment.

Specifically, a set of local 3D Gaussians $\mathcal{G}^f = \{G_i^f\}_{i=1}^m$ is initialized based on the results from fragment registration. These local Gaussians are progressively merged into larger sets through a pairwise process. However, naive pairwise merging introduces two key challenges: an excessive number of Gaussians for optimization and inconsistencies between different local Gaussian sets. To overcome these issues, we propose a hierarchical pipeline that iteratively performs local Gaussian optimization, cross-fragment alignment, and visibility masking for pairwise merging, culminating in a globally consistent 3D scene.

Local 3D Gaussian Construction We initialize a distinct set of Gaussians for each fragment, resulting in a sequence of Gaussian sets $\mathcal{G}^f = \{G_i^f\}_{i=1}^m$, where G_i^f is initialized from fragment \mathcal{I}_i^f .

In the fragment registration stage, we obtain the dense point cloud for the key frame, along with the relative pose and scale for other frames in the fragment. Using this information, we create a locally consistent dense point cloud by applying the same scale across the entire point map generated by MAST3R. To initialize G_i^f , we assign a Gaussian to each point in the pixel-wise point cloud, setting its attributes as follows: color based on the corresponding pixel, center at the 3D point location, opacity adhering to the 3D-GS protocol [18], and scaling such that it projects as a one-pixel radius in the 2D image (achieved by dividing the depth by the focal length). Here we set the Gaussians as isotropic to reduce the degrees of freedom in Gaussian training.

Since the initial camera poses and point cloud positions may contain minor inaccuracies, we further refine them through joint optimization of camera poses and Gaussian parameters. Specifically, for each local Gaussian in G_i^f , we randomly sample frames within the fragment, render the current Gaussians into sampled frame, and backpropagate gradient updates to the Gaussian positions, colors, scales, opacities, and camera poses.

Hierarchical Merging with Cross Fragment Alignment

To achieve a globally consistent 3D reconstruction for the entire video, we integrate the sequence of local 3D Gaussian sets \mathcal{G}^f , each initialized and optimized independently within disjoint fragments, into a cohesive representation. To mitigate incremental error accumulation and manage the

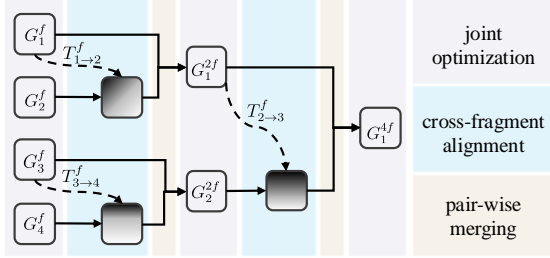


Figure 3. **Hierarchical Gaussian Alignment.** The process iteratively performs three stages: 1) joint optimization of camera poses and local Gaussians (purple), 2) cross-fragment alignment for new local Gaussian (blue), and 3) visibility masking and pair-wise merging of local Gaussians (yellow), until a globally consistent scene reconstruction is achieved.

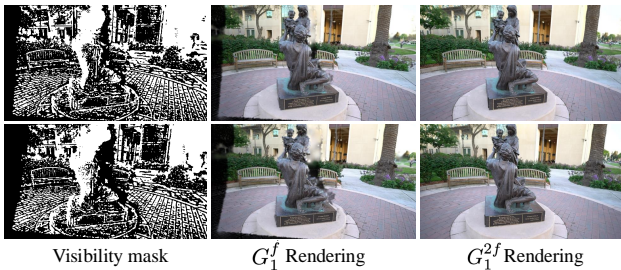


Figure 4. **Visibility Mask** showing rendering G_1^f into next two novel frames in G_2^f . White region denotes pixels faithful reconstruction using G_1^f , while black represents pixels unseen from G_1^f . With visibility mask, we select complementary gaussians from G_2^f , merging them with G_1^f into G_1^{2f} .

number of Gaussians during merging, we employ a hierarchical merging strategy as illustrated in Fig. 3.

To merge independently optimized G_1^f and G_2^f , we first perform **cross-fragment alignment**, using G_1^f as the reference coordinate system. Within each fragment, the first frame (key frame) has an identity pose, while other frames are defined by their relative poses to the key frame. Using the initial transformation $T_{1 \rightarrow 2}^f$, we compute the camera poses for the novel frames covered by G_2^f . By enforcing photometric loss on the next novel view while freezing all parameters in G_1^f , we could further optimize $T_{1 \rightarrow 2}^f$ into $T_{1 \rightarrow 2}^{f*}$. Then, we align the Gaussians in G_2^f with the coordinate system of G_1^f by using $T_{1 \rightarrow 2}^{f* -1}$.

To avoid duplicating Gaussians in regions where G_1^f already provides adequate scene geometry representation on novel view, we use a **visibility mask** to determine areas that G_1^f could faithfully reconstruct:

$$M(\mathbf{p}) = \text{Conf}(\mathbf{p}) > \beta + D(\mathbf{p}) > 0, \quad (3)$$

where \mathbf{p} represents pixel position on image plane, $D(\mathbf{p})$ is rendered depth. $\text{Conf}(\mathbf{p})$ is the rendered confidence, e.g. if

a pixel contains information from the current gaussian, and threshold β determines the masking criteria.

As in Fig. 4, the visibility mask effectively identifies regions where Gaussians from G_1^f could provide sufficient depth and confidence. Importantly, the mask remains robust to occlusions, even when covered by large Gaussians. Since our initialization is pixel-wise point clouds, the inverse of the visibility mask can be directly applied to G_2^f to select Gaussians that complement the missing regions of G_1^f . These selected Gaussians inherit previously optimized parameters, ensuring seamless integration into the unified representation.

After merging pair of local Gaussians, further **joint optimization** is needed to ensure the merged Gaussian set G_1^{2f} meets our consistency objectives. We jointly optimize Gaussian properties and camera poses for G_1^{2f} . Specifically, we randomly sample frames within $[I_1, I_8]$, render all Gaussians into each frame, and backpropagate gradients to Gaussian positions, colors, scales, opacities, and camera poses.

4. Experiments

4.1. Experimental Setup

Datasets We carry out comprehensive experiments using various real-world datasets, including Tanks and Temples [19], CO3D-V2 [31]. For Tanks and Temples, following NoPe-NeRF [6] and CF-3DGS [12], we assess both novel view synthesis quality and pose estimation accuracy across 8 scenes, which span both indoor and outdoor environments. In each case, we use 7 out of every 8 frames from the video clips as training data and evaluate the novel view synthesis on the remaining frame except Family. For CO3D-V2, which contains thousands of object-centric videos where the camera orbits the object, recovering camera poses is significantly more challenging due to the complex and large camera motions. We follow the protocol of CF-3DGS [12] to choose the same 10 scenes from different object categories and apply the same procedure to divide the dataset into training and testing sets.

Metrics We assess our approach on two key tasks using benchmark datasets [19, 24, 31]: generating novel views and estimating camera poses. For the task of novel view synthesis, we evaluate performance using common metrics such as Peak Signal-to-Noise Ratio (PSNR), Structural Similarity Index (SSIM) [41], and Learned Perceptual Image Patch Similarity (LPIPS) [45]. In terms of camera pose estimation, we evaluate Absolute Trajectory Error (ATE) [38] and utilize COLMAP-generated poses from all dense views as our ground-truth for evaluation. While Relative Pose Error (RPE) [38] evaluates the local consistency of relative transformations between consecutive frames, it can be sensitive to discrepancies in intrinsic parameters such

	Camera Param.	Train Time	SSIM \uparrow	PSNR \uparrow	LPIPS \downarrow	ATE \downarrow
3DGS [18]	GT K & Pose	\sim 50min	0.9175	30.20	0.1025	-
NeRF-mm [42]	-	\sim 13h33min	0.5313	20.02	0.5450	0.035
BARF [21]	GT K	\sim 20h	0.6075	23.42	0.5362	0.078
NoPe-NeRF [6]	GT K	\sim 30h	0.7125	25.49	0.4113	0.013
CF-3DGS [12]	GT K	\sim 2h20min	0.9213	31.14	0.0859	0.004
Ours	-	26min20s	0.9347	31.59	0.0730	0.004

Table 1. **Quantitative Evaluations on Tanks and Temples Dataset.** Our method achieves superior rendering quality and pose accuracy while requiring minimal training time and no camera parameters. (-) indicates no camera parameters required, GT K indicates known intrinsics, GT K & Pose indicates both known intrinsics and extrinsics. The best results are highlighted in bold.

as focal length. However, ATE provides a more comprehensive measure of global trajectory accuracy and is better aligned with the goals of our method, which emphasizes globally consistent 3D reconstruction [38]. As such, we prioritize ATE as the primary metric for evaluating the poses of `VideoLifter`.

Implementation Details Our implementation is built on the PyTorch platform. During fragment registration, each fragment consists of $k = 4$ frames. For depth map prediction, we utilize MAST3R with a resolution of 512 on the longer side. We run 200 iterations for key frame optimization. For hierarchical Gaussian alignment, we initialize each local Gaussian using the number of pixels within the fragment and train it for 200 steps. Camera poses are represented in quaternion format. For pair-wise merging, the transformation matrix from key frame optimization is applied to the camera poses and Gaussian points of the subsequent local Gaussian. First, the camera poses are optimized with a learning rate of $1e-3$ for 200 steps. Next, a mask is rendered to identify inadequately reconstructed regions, where new Gaussians are added. This process is repeated iteratively until a globally consistent Gaussian representation is achieved. We uniformly sample $\frac{1}{2}$ and $\frac{1}{4}$ training views on Tanks and Temples and CO3D-V2, respectively. All experiments were conducted on a single Nvidia A6000 GPU to maintain fair comparison.

4.2. Quantitative Evaluations

To quantitatively evaluate the quality of synthesized novel views, we present the results in Tab. 1 for the Tanks and Temples dataset and Tab. 2 for the CO3D-V2 dataset. Baseline models were re-trained using their officially released code to ensure a fair comparison of training time. Compared to other self-calibrating radiance field methods, our approach achieves superior performance in terms of efficiency and rendering quality, which is largely thanks to our decoupled fragment registration and hierarchical alignment process. Compared to the most relevant baseline CF-3DGS [12], we reduce $>80\%$ training time yet get >0.012 LPIPS improvement on Tanks and Temples, and

reduce $>85\%$ training time yet get >0.12 LPIPS improvement on CO3D-V2 dataset. Note that our `VideoLifter` does not require any ground-truth camera parameters, making it more adaptable to scenes that do not have or fail to get precomputed intrinsics from COLMAP. Compared to NeRFmm [42], which also does not need ground-truth camera parameters, our `VideoLifter` delivers much better quality and much less training time. Detailed per-scene breakdown results could be found in the Supplementary.

4.3. Qualitative Evaluations

As shown in Fig. 5, for large-scale scenes from the Tanks and Temples dataset, thanks to the hierarchical design in `VideoLifter`, our method consistently produces sharper details among all test views, and preserves fine details that are well-optimized within each fragment. For the CO3D-V2 dataset, which includes 360-degree scenes with complex trajectories, achieving a globally consistent 3D reconstruction without any COLMAP initialization is even more challenging. Baselines that rely on monocular depth prediction to unproject images into point clouds often suffer from depth scale inconsistencies, making them fragile and prone to failure. Even CF-3DGS, which uses the more robust ZoeDepth monocular depth estimator [5], encounters severe failures on CO3D-V2. In contrast, `VideoLifter` leverages 3D geometry priors to achieve robust registration, making it highly adaptable and resilient in challenging settings. More results could be found in the Supplementary.

4.4. Ablation Study

We conducted a series of ablation studies to validate the effectiveness of our design choices in `VideoLifter`, transitioning from an all-at-once optimization approach using MVS as initialization to a structured two-stage pipeline with hierarchical Gaussian alignment. Results are in Tab. 3.

Quality of directly using MAST3R MVS as initialization? We assess the accuracy of camera poses derived from the MVS point map. As illustrated in row 1 and row 8, there exists considerable scope for enhancing the MVS-initialized scene geometry.

Effect of decomposing the reconstruction pipeline

	Camera Param.	Train Time	SSIM \uparrow	PSNR \uparrow	LPIPS \downarrow	ATE \downarrow
NeRF-mm [42]	-	\sim 17h22min	0.4380	13.43	0.7058	0.061
NoPe-NeRF [6]	GT K	\sim 35h	0.7030	25.54	0.5190	0.055
CF-3DGS [12]	GT K	\sim 2h55min	0.6821	22.98	0.3515	0.014
Ours	-	24min58s	0.8502	28.37	0.2237	0.012

Table 2. **Quantitative Evaluations on CO3D-V2 Datasets.** Our method significantly decreases training time in CO3D-V2. (-) indicates no camera parameters required, GT K indicates known intrinsics. The best results are highlighted in bold.

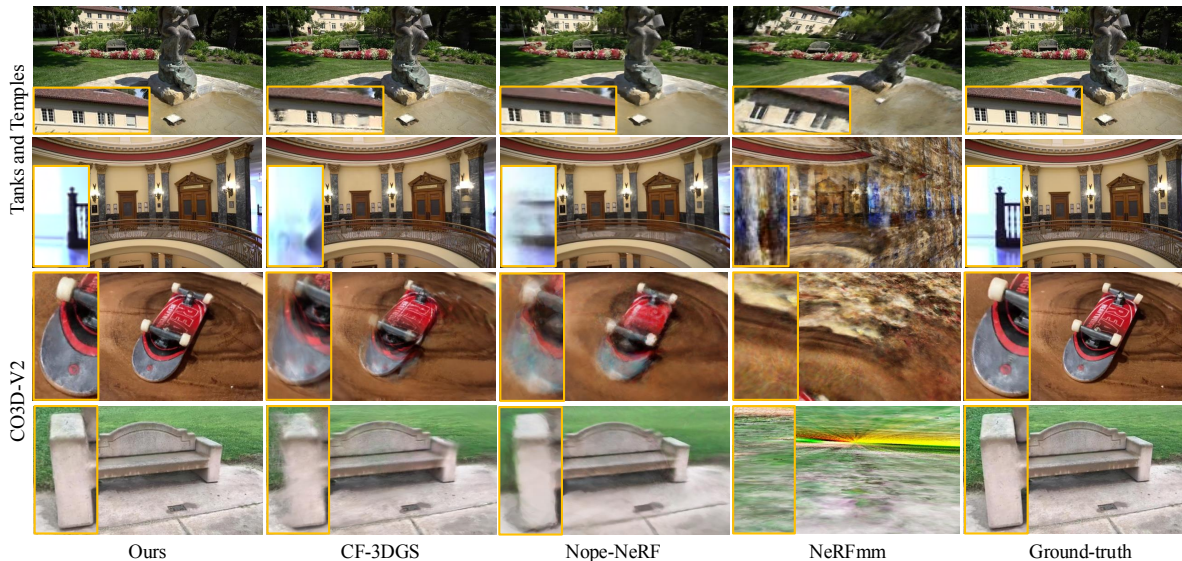


Figure 5. **Visual Comparisons** between VideoLifter and other baselines. The insets highlight the details of renderings. VideoLifter achieves faithful 3D reconstruction, preserves better details, and alleviates incremental error in progressive learning.

#	Method	Train Time	SSIM \uparrow	PSNR \uparrow	LPIPS \downarrow
1	MASt3R MVS initialization	35min	0.8582	27.91	0.1768
2	No Decomposition	30min15s	0.7563	23.03	0.3515
3	No Hierarchy	53min12s	0.6969	20.22	0.3876
4	$k = 2$	35min2s	0.8936	29.77	0.2138
5	$k = 8$	38min5s	0.8787	27.51	0.2743
6	$\beta = 0.5$	23min18s	0.6529	18.50	0.4457
7	$\beta = 0.99$	43min55s	0.8325	29.08	0.2691
8	Ours ($k = 4, \beta = 0.9$)	28min49s	0.8957	30.02	0.1745

Table 3. **Ablation studies on 34_1403_4393 scene from CO3D-V2 Dataset.** k denotes the number of frames in local fragment. β denotes the rendering confidence threshold in gaussian merging.

into two stages? As in row 2 and row 8, decomposing a monolithic pipeline into two stages could disentangle the problem and simplify the optimization of scene reconstruction and camera pose.

Hierarchical Gaussian alignment design? As in row 3 and row 8, it confirms that the progressive merging of local Gaussian representations significantly reduces drift, achieving more globally consistent reconstructions across extended video sequences.

Effect of different sizes for local fragments? Smaller fragments yielded more precise local alignment but in-

creased computational overhead, while larger fragments reduced processing time at the cost of minor accuracy loss. We selected an optimal fragment size as 4 to balance computational efficiency and alignment accuracy.

Effect of different threshold of rendering confidence?

A smaller β allows fewer new Gaussians to merge into the current local Gaussian and degrades the performance, while a too-high β adds too many Gaussians and makes the training slower and harder. To balance the number of Gaussians and training time, we set $\beta = 0.9$ by default.

5. Conclusion

We introduced VideoLifter, a framework that efficiently reconstructs 3D scenes from monocular video without requiring pre-computed camera poses or predefined intrinsics. VideoLifter leverages learning-based stereo priors for initial sparse scene reconstruction and incorporates a hierarchical alignment approach with 3D Gaussian splatting to produce dense, globally consistent models. Compared to previous state-of-the-art methods [6, 12], VideoLifter achieves high-quality reconstructions from casual video, reducing computational demand.

References

- [1] Shai Avidan and Amnon Shashua. Novel view synthesis in tensor space. In *Proceedings of IEEE Computer Society Conference on Computer Vision and Pattern Recognition*, pages 1034–1040. IEEE, 1997. 2
- [2] Jonathan T. Barron, Ben Mildenhall, Dor Verbin, Pratul P. Srinivasan, and Peter Hedman. Mip-NeRF 360: Unbounded Anti-Aliased Neural Radiance Fields. *2022 IEEE/CVF Conference on Computer Vision and Pattern Recognition (CVPR)*, pages 5460–5469, 2022. 2
- [3] Jonathan T Barron, Ben Mildenhall, Dor Verbin, Pratul P Srinivasan, and Peter Hedman. Mip-nerf 360: Unbounded anti-aliased neural radiance fields. In *Proceedings of the IEEE/CVF Conference on Computer Vision and Pattern Recognition*, pages 5470–5479, 2022.
- [4] Jonathan T Barron, Ben Mildenhall, Dor Verbin, Pratul P Srinivasan, and Peter Hedman. Zip-nerf: Anti-aliased grid-based neural radiance fields. In *Proceedings of the IEEE/CVF International Conference on Computer Vision*, pages 19697–19705, 2023. 2
- [5] Shariq Farooq Bhat, Reiner Birkl, Diana Wofk, Peter Wonka, and Matthias Müller. Zoedepth: Zero-shot transfer by combining relative and metric depth. *arXiv preprint arXiv:2302.12288*, 2023. 7
- [6] Wenjing Bian, Zirui Wang, Kejie Li, Jia-Wang Bian, and Victor Adrian Prisacariu. Nope-nerf: Optimising neural radiance field with no pose prior. In *Proceedings of the IEEE/CVF Conference on Computer Vision and Pattern Recognition*, pages 4160–4169, 2023. 2, 3, 6, 7, 8
- [7] Zhang Chen, Zhong Li, Liangchen Song, Lele Chen, Jingyi Yu, Junsong Yuan, and Yi Xu. Neurf: A neural fields representation with adaptive radial basis functions. In *Proceedings of the IEEE/CVF International Conference on Computer Vision*, pages 4182–4194, 2023. 2
- [8] Zezhou Cheng, Carlos Esteves, Varun Jampani, Abhishek Kar, Subhransu Maji, and Ameesh Makadia. Lu-nerf: Scene and pose estimation by synchronizing local unposed nerfs. In *Proceedings of the IEEE/CVF International Conference on Computer Vision*, pages 18312–18321, 2023. 3
- [9] Jakob Engel, Thomas Schöps, and Daniel Cremers. Lsdslam: Large-scale direct monocular slam. In *European conference on computer vision*, pages 834–849. Springer, 2014. 3
- [10] Zhiwen Fan, Wenyan Cong, Kairun Wen, Kevin Wang, Jian Zhang, Xinghao Ding, Danfei Xu, Boris Ivanovic, Marco Pavone, Georgios Pavlakos, et al. Instantsplat: Unbounded sparse-view pose-free gaussian splatting in 40 seconds. *arXiv preprint arXiv:2403.20309*, 2024. 3
- [11] Martin A Fischler and Robert C Bolles. Random sample consensus: a paradigm for model fitting with applications to image analysis and automated cartography. *Communications of the ACM*, 24(6):381–395, 1981. 5
- [12] Yang Fu, Sifei Liu, Amey Kulkarni, Jan Kautz, Alexei A Efros, and Xiao-long Wang. Colmap-free 3d gaussian splatting. *arXiv preprint arXiv:2312.07504*, 2023. 2, 3, 6, 7, 8
- [13] Yasutaka Furukawa, Brian Curless, Steven M Seitz, and Richard Szeliski. Towards internet-scale multi-view stereo. In *2010 IEEE computer society conference on computer vision and pattern recognition*, pages 1434–1441. IEEE, 2010. 3
- [14] Riccardo Gherardi, Michela Farenzena, and Andrea Fusiello. Improving the efficiency of hierarchical structure-and-motion. In *2010 IEEE Computer Society Conference on Computer Vision and Pattern Recognition*, pages 1594–1600. IEEE, 2010. 3
- [15] Xufeng Han, Thomas Leung, Yangqing Jia, Rahul Sukthankar, and Alexander C. Berg. Matchnet: Unifying feature and metric learning for patch-based matching. In *2015 IEEE Conference on Computer Vision and Pattern Recognition (CVPR)*, pages 3279–3286, 2015. 3
- [16] Yoonwoo Jeong, Seokjun Ahn, Christopher Choy, Anima Anandkumar, Minsu Cho, and Jaesik Park. Self-calibrating neural radiance fields. In *Proceedings of the IEEE/CVF International Conference on Computer Vision*, pages 5846–5854, 2021. 3
- [17] Kaiwen Jiang, Yang Fu, Yash Belhe, Xiaolong Wang, Hao Su, Ravi Ramamoorthi, et al. A construct-optimize approach to sparse view synthesis without camera pose. *arXiv preprint arXiv:2405.03659*, 2024. 3
- [18] Bernhard Kerbl, Georgios Kopanas, Thomas Leimkühler, and George Drettakis. 3d gaussian splatting for real-time radiance field rendering. *ACM Transactions on Graphics (TOG)*, 42(4):1–14, 2023. 1, 2, 3, 5, 7
- [19] Arno Knapitsch, Jaesik Park, Qian-Yi Zhou, and Vladlen Koltun. Tanks and temples: Benchmarking large-scale scene reconstruction. *ACM Transactions on Graphics (TOG)*, 36(4):1–13, 2017. 6
- [20] Vincent Leroy, Johann Cabon, and Jérôme Revaud. Grounding image matching in 3d with mast3r. *arXiv preprint arXiv:2406.09756*, 2024. 2, 4
- [21] Chen-Hsuan Lin, Wei-Chiu Ma, Antonio Torralba, and Simon Lucey. Barf: Bundle-adjusting neural radiance fields. In *Proceedings of the IEEE/CVF International Conference on Computer Vision*, pages 5741–5751, 2021. 2, 3, 7
- [22] David G Lowe. Distinctive image features from scale-invariant keypoints. *International journal of computer vision*, 60(2):91–110, 2004. 3
- [23] Jinjie Mai, Wenxuan Zhu, Sara Rojas, Jesus Zarzar, Abdullah Hamdi, Guocheng Qian, Bing Li, Silvio Giancola, and Bernard Ghanem. Trackerf: Bundle adjusting nerf from sparse and noisy views via feature tracks. *arXiv preprint arXiv:2408.10739*, 2024. 3
- [24] Andreas Meuleman, Yu-Lun Liu, Chen Gao, Jia-Bin Huang, Changil Kim, Min H Kim, and Johannes Kopf. Progressively optimized local radiance fields for robust view synthesis. In *Proceedings of the IEEE/CVF Conference on Computer Vision and Pattern Recognition*, pages 16539–16548, 2023. 2, 3, 6
- [25] Ben Mildenhall, Pratul P Srinivasan, Rodrigo Ortiz-Cayon, Nima Khademi Kalantari, Ravi Ramamoorthi, Ren Ng, and Abhishek Kar. Local light field fusion: Practical view synthesis with prescriptive sampling guidelines. *ACM Transactions on Graphics (TOG)*, 38(4):1–14, 2019. 2
- [26] Ben Mildenhall, Pratul P Srinivasan, Matthew Tancik, Jonathan T Barron, Ravi Ramamoorthi, and Ren Ng. Nerf:

- Representing Scenes As Neural Radiance Fields for View Synthesis. *Communications of the ACM*, 65(1):99–106, 2021. 1, 2
- [27] Pierre Moulon, Pascal Monasse, and Renaud Marlet. Global fusion of relative motions for robust, accurate and scalable structure from motion. In *Proceedings of the IEEE international conference on computer vision*, pages 3248–3255, 2013. 2
- [28] Raul Mur-Artal, Jose Maria Martinez Montiel, and Juan D Tardos. Orb-slam: a versatile and accurate monocular slam system. *IEEE transactions on robotics*, 31(5):1147–1163, 2015. 3
- [29] Richard A Newcombe, Steven J Lovegrove, and Andrew J Davison. Dtam: Dense tracking and mapping in real-time. In *2011 international conference on computer vision*, pages 2320–2327. IEEE, 2011. 3
- [30] Eric Penner and Li Zhang. Soft 3D Reconstruction for View Synthesis. *ACM Transactions on Graphics (TOG)*, 36(6):1–11, 2017. 2
- [31] Jeremy Reizenstein, Roman Shapovalov, Philipp Henzler, Luca Sbordone, Patrick Labatut, and David Novotny. Common objects in 3d: Large-scale learning and evaluation of real-life 3d category reconstruction. In *Proceedings of the IEEE/CVF international conference on computer vision*, pages 10901–10911, 2021. 6
- [32] Johannes L Schonberger and Jan-Michael Frahm. Structure-from-motion revisited. In *Proceedings of the IEEE conference on computer vision and pattern recognition*, pages 4104–4113, 2016. 1, 2, 3
- [33] Steven M Seitz and Charles R Dyer. Photorealistic Scene Reconstruction by Voxel Coloring, 2002. US Patent 6,363,170. 2
- [34] Heung-Yeung Shum, Qifa Ke, and Zhengyou Zhang. Efficient bundle adjustment with virtual key frames: A hierarchical approach to multi-frame structure from motion. In *Proceedings. 1999 IEEE computer society conference on computer vision and pattern recognition (Cat. No PR00149)*, pages 538–543. IEEE, 1999. 2
- [35] Noah Snavely. Scene reconstruction and visualization from internet photo collections: A survey. *IPSI Transactions on Computer Vision and Applications*, 3:44–66, 2011. 3
- [36] Pratul P Srinivasan, Richard Tucker, Jonathan T Barron, Ravi Ramamoorthi, Ren Ng, and Noah Snavely. Pushing the Boundaries of View Extrapolation With Multiplane Images. In *Proceedings of the IEEE/CVF Conference on Computer Vision and Pattern Recognition*, pages 175–184, 2019. 2
- [37] Pratul P Srinivasan, Ben Mildenhall, Matthew Tancik, Jonathan T Barron, Richard Tucker, and Noah Snavely. Lighthouse: Predicting Lighting Volumes for Spatially-Coherent Illumination. In *Proceedings of the IEEE/CVF Conference on Computer Vision and Pattern Recognition*, pages 8080–8089, 2020. 2
- [38] Jürgen Sturm, Nikolas Engelhard, Felix Endres, Wolfram Burgard, and Daniel Cremers. A benchmark for the evaluation of rgb-d slam systems. In *2012 IEEE/RSJ international conference on intelligent robots and systems*, pages 573–580. IEEE, 2012. 6, 7
- [39] Prune Truong, Marie-Julie Rakotosaona, Fabian Manhardt, and Federico Tombari. Sparf: Neural radiance fields from sparse and noisy poses. In *Proceedings of the IEEE/CVF Conference on Computer Vision and Pattern Recognition*, pages 4190–4200, 2023. 3
- [40] Shuzhe Wang, Vincent Leroy, Yann Cabon, Boris Chidlovskii, and Jerome Revaud. Dust3r: Geometric 3d vision made easy. In *Proceedings of the IEEE/CVF Conference on Computer Vision and Pattern Recognition*, pages 20697–20709, 2024. 3
- [41] Zhou Wang, Alan C Bovik, Hamid R Sheikh, and Eero P Simoncelli. Image quality assessment: from error visibility to structural similarity. *IEEE transactions on image processing*, 13(4):600–612, 2004. 6
- [42] Zirui Wang, Shangzhe Wu, Weidi Xie, Min Chen, and Victor Adrian Prisacariu. Nerf-: Neural radiance fields without known camera parameters. *arXiv preprint arXiv:2102.07064*, 2021. 2, 3, 7, 8
- [43] Changchang Wu et al. Visualsfm: A visual structure from motion system, 2011. URL <http://www.cs.washington.edu/homes/ccwu/vsfm>, 14:2, 2011. 3
- [44] Qiangeng Xu, Zexiang Xu, Julien Philip, Sai Bi, Zhixin Shu, Kalyan Sunkavalli, and Ulrich Neumann. Point-nerf: Point-based neural radiance fields. In *Proceedings of the IEEE/CVF conference on computer vision and pattern recognition*, pages 5438–5448, 2022. 2
- [45] Richard Zhang, Phillip Isola, Alexei A Efros, Eli Shechtman, and Oliver Wang. The unreasonable effectiveness of deep features as a perceptual metric. In *Proceedings of the IEEE conference on computer vision and pattern recognition*, pages 586–595, 2018. 6
- [46] Matthias Zwicker, Hanspeter Pfister, Jeroen Van Baar, and Markus Gross. Ewa volume splatting. In *Proceedings Visualization, 2001. VIS'01.*, pages 29–538. IEEE, 2001. 2